

# On the Structural Stability of Melt Spun Ribbons of $\text{Fe}_{95-x}\text{Zr}_x\text{B}_4\text{Cu}_1$ ( $x = 7$ and $9$ ) Alloys and Correlation with Their Magnetic Properties



D. ARVINDHA BABU, BHASKAR MAJUMDAR, RAJDEEP SARKAR, B.S. MURTY, and K. CHATTOPADHYAY

Melt spun ribbons of  $\text{Fe}_{95-x}\text{Zr}_x\text{B}_4\text{Cu}_1$  with  $x = 7$  (Z7B4) and  $9$  (Z9B4) alloys have been prepared, and their structure and magnetic properties have been evaluated using XRD, DSC, TEM, VSM, and Mössbauer spectroscopy. The glass forming ability (GFA) of both alloys has been calculated theoretically using thermodynamical parameters, and Z9B4 alloy is found to possess higher GFA than that of Z7B4 alloy which is validated by XRD results. On annealing, the amorphous Z7B4 ribbon crystallizes into nanocrystalline  $\alpha$ -Fe, whereas amorphous Z9B4 ribbon shows two-stage crystallization process, first partially to bcc solid solution which is then transformed to nanocrystalline  $\alpha$ -Fe and  $\text{Fe}_2\text{Zr}$  phases exhibiting bimodal distribution. A detailed phase analysis using Mössbauer spectroscopy through hyperfine field distribution of phases has been carried out to understand the crystallization behavior of Z7B4 and Z9B4 alloy ribbons. In order to understand the phase transformation behavior of Z7B4 and Z9B4 ribbons, molar Gibbs free energies of amorphous,  $\alpha$ -Fe, and  $\text{Fe}_2\text{Zr}$  phases have been evaluated. It is found that in case of Z7B4,  $\alpha$ -Fe is always a stable phase, whereas  $\text{Fe}_2\text{Zr}$  is stable at higher temperature for Z9B4.

DOI: 10.1007/s11661-015-3204-x

© The Minerals, Metals & Materials Society and ASM International 2015

## I. INTRODUCTION

$\text{Fe}_{88}\text{Z}_7\text{B}_4\text{Cu}_1$  (NANOPERM) alloys with improved soft magnetic properties developed by Suzuki *et al.*<sup>[1]</sup> exhibit unique combination of soft magnetic properties such as high saturation, high Curie temperature, high permeability, low coercivity, and high resistivity which are superior to other conventional soft magnetic materials. The ultra-soft magnetic properties arises in these materials due to the coexistence of amorphous and nanograins. According to random anisotropy theory, the exchange coupling between nanocrystalline grains and amorphous matrix results in averaging out of magnetocrystalline anisotropy which forces the magnetization vector to be aligned parallel to

the field direction.<sup>[2]</sup> The saturation magnetostriction becomes almost zero due to the positive and negative contributions from the amorphous and nanocrystalline phases, respectively.<sup>[3]</sup> These alloys are generally processed by rapid solidification (melt spinning) method to produce an amorphous phase followed by controlled heat treatment to obtain nanocrystalline precipitates in amorphous matrix.

Our earlier work has shown that, on decreasing the wheel speed (lower cooling rate), the structure of  $\text{Fe}_{88}\text{Z}_7\text{B}_4\text{Cu}_1$  alloy changes from completely amorphous phase to the cellular structure of bcc solid solution coexisting with the amorphous phase at the intercellular region, thus affecting the soft magnetic properties in the as-spun condition.<sup>[4]</sup> Shih *et al.*<sup>[5]</sup> have estimated the volume fraction of nanocrystalline bcc  $\alpha$ -Fe phase, residual amorphous phase, and  $\text{Fe}_{23}\text{Zr}_6$  phase in melt spun ribbon of  $\text{Fe}_{89}\text{Z}_7\text{B}_3\text{Cu}_1$  alloy annealed at 898 K (625 °C) using Mössbauer technique and also reported that these estimates are consistent with atom probe study reported by Hono.<sup>[6]</sup> In a similar way, Mössbauer technique was used by us to find out the composition and volume fraction of nanocrystalline bcc  $\alpha$ -Fe(Co) phase in  $(\text{Fe}_{1-x}\text{Co}_x)_{88}\text{Z}_7\text{B}_4\text{Cu}_1$  melt spun ribbons in an earlier report.<sup>[7]</sup>

Recently, we have reported the structure and soft magnetic properties of two series of alloys, namely  $\text{Fe}_{99-x-y}\text{Zr}_x\text{B}_y\text{Cu}_1$  with  $x + y = 11$  and  $x + y = 13$ .<sup>[8]</sup> In this study, the glass forming ability (GFA) of the alloys has been calculated based on thermodynamic properties and verified with experimental results. Moreover, a soft magnetic property vs Zr concentration map has been

D. ARVINDHA BABU, Scientist, is with the Advanced Magnetics Group, Defence Metallurgical Research Laboratory, Defence Research and Development Organization, Kanchanbagh, Hyderabad 500058, India, and also with the Department of Metallurgical and Materials Engineering, Indian Institute of Technology Madras, Chennai 600036, India. BHASKAR MAJUMDAR, Scientist, is with the Advanced Magnetics Group, Defence Metallurgical Research Laboratory, Defence Research and Development Organization. RAJDEEP SARKAR, Scientist, is with the Electron Microscopy group, Defence Metallurgical Research Laboratory, Defence Research and Development Organization. Contact e-mail: bhaskarmajumdar1@gmail.com, bhaskar@dmrl.drdo.in B.S. MURTY, Professor, is with the Department of Metallurgical and Materials Engineering, Indian Institute of Technology Madras. K. CHATTOPADHYAY, Professor, is with the Department of Materials Engineering, Indian Institute of Science, Bangalore 560012, India.

Manuscript submitted May 27, 2015.

Article published online November 17, 2015

established and alloys having better soft magnetic properties have been identified. Interestingly, it was found that  $\text{Fe}_{86}\text{Zr}_9\text{B}_4\text{Cu}_1$  (Z9B4) alloy has very low coercivity and low saturation magnetization in the as-spun condition. Unlike other alloys, upon annealing, the coercivity increases drastically and saturation magnetization increases gradually. In this paper, we also report a detailed study on phase transformation behavior of amorphous  $\text{Fe}_{86}\text{Zr}_9\text{B}_4\text{Cu}_1$  (Z9B4) ribbon and compare the results with  $\text{Fe}_{88}\text{Zr}_7\text{B}_4\text{Cu}_1$  (Z7B4) ribbon which has been studied extensively. Thermodynamic calculations have been carried out for understanding the stability of the phases.

## II. EXPERIMENTAL DETAILS

Two alloys of nominal compositions  $\text{Fe}_{88}\text{Zr}_7\text{B}_4\text{Cu}_1$  (termed as Z7B4) and  $\text{Fe}_{86}\text{Zr}_9\text{B}_4\text{Cu}_1$  (termed as Z9B4) have been prepared by melting the eutectic Fe-Zr master alloy together with high-purity Fe, B, and Cu in a vacuum induction furnace ( $2 \times 10^{-4}$  mbar). Rapidly solidified ribbons (2 to 5 mm wide and 30 to 100  $\mu\text{m}$  thick) of all alloys were produced in an argon atmosphere using a vacuum melt spinner (initially evacuated up to a vacuum level of  $1 \times 10^{-4}$  mbar) at different wheel speed conditions. All ribbons were then vacuum annealed ( $2 \times 10^{-5}$  mbar) at different temperatures ranging from 773 K to 858 K (500 °C to 585 °C) for 1 hour.

Structure of the as-spun and annealed ribbons was determined by X-ray diffractometer (PHILIPS PW1830 XRD) using  $\text{Cu-K}\alpha$  ( $\lambda = 1.54056 \text{ \AA}$ ) radiation. A differential scanning calorimeter (NETSCH STA 409 PC DSC) was used to evaluate the thermal stability of the as-spun ribbons. Microstructural characterization was carried out using transmission electron microscope (FEI Tecnai-20UT TEM). Mössbauer experiments were carried out using a constant acceleration spectrometer (FAST ComTech, Germany) in transmission mode with 25 mCi,  $^{57}\text{Co}$ (Rh) source. Thermomagnetic curves for the as-spun ribbons have been measured using a vibrating sample magnetometer (ADE EV7 VSM) with an interval of 5 K (5 °C) equilibrating for 3 seconds up to 823 K (550 °C), keeping a constant field of 500 Oe.

## III. RESULTS

### A. Structural Evolution

Figures 1(a) and (b) show the XRD patterns of melt spun Z7B4 and Z9B4 ribbons, respectively, with increasing order of thickness obtained by reducing the wheel speed. XRD pattern of 30- $\mu\text{m}$ -thick Z7B4 ribbon (Figure 1(a)) exhibits fully amorphous phase, whereas for 40- $\mu\text{m}$ -thick ribbon, the coexistence of bcc  $\alpha$ -Fe phase along with amorphous phase can be observed. In case of Z9B4 ribbon (Figure 1(b)), the XRD patterns exhibit fully amorphous phase even up to a ribbon thickness of 100  $\mu\text{m}$ . This experimentally proves that the Z9B4 ribbon has better GFA than that of Z7B4. The GFA of these alloys were calculated theoretically using a recent approach, proposed by Rao *et al.*<sup>[9]</sup> Accordingly,

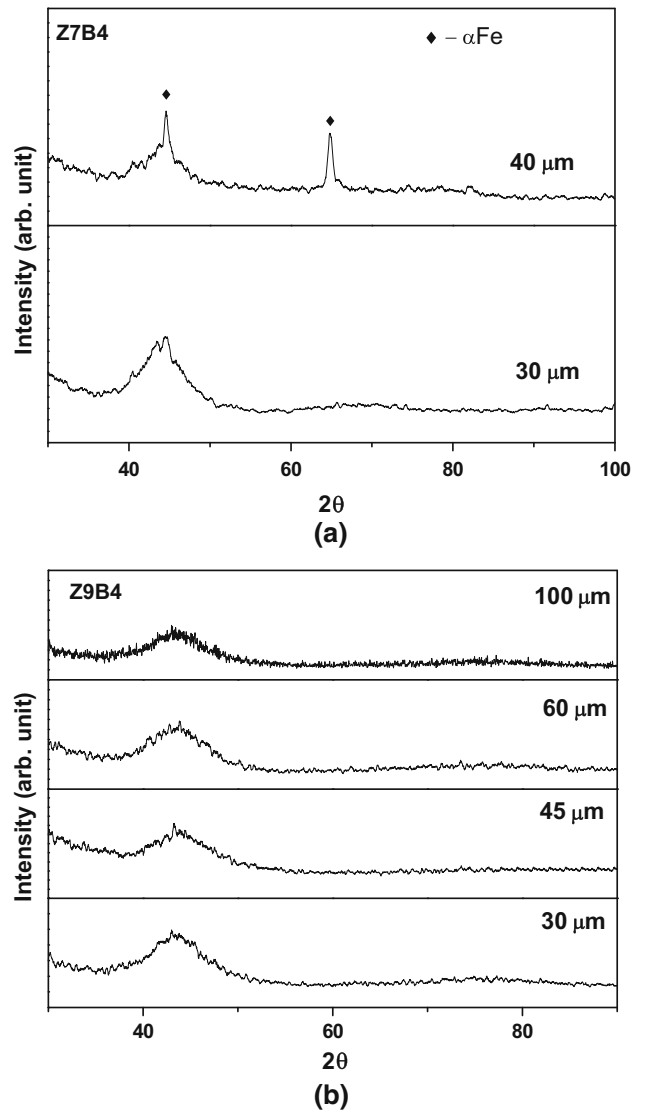


Fig. 1—XRD patterns of the as-spun ribbons prepared at different wheel speeds of (a) Z7B4 and (b) Z9B4 alloys.

thermodynamic and topological models are combined to evolve a parameter,  $P_{\text{HSS}}$ , which is defined as

$$P_{\text{HSS}} = \Delta H^{\text{chem}}(\Delta S_{\sigma}/k_{\text{B}})(\Delta S_{\text{C}}/R), \quad [1]$$

where  $\Delta H^{\text{chem}}$  is the enthalpy of chemical mixing,  $\Delta S_{\sigma}$  is the mismatch entropy,  $\Delta S_{\text{C}}$  is the configurational entropy,  $R$  is the gas constant, and  $k_{\text{B}}$  is Boltzmann constant. It was reported that the parameter,  $P_{\text{HSS}}$ , correlates well with the GFA of bulk glass forming alloy systems.<sup>[10,11]</sup> The  $P_{\text{HSS}}$  values of Z7B4 and Z9B4 alloys are  $-0.78$  and  $-0.88$  kJ/mol, respectively, revealing that Z9B4 alloy (more negative) has higher GFA than that of Z7B4.

For further investigation on structure and soft magnetic properties of the as-spun and annealed ribbons, only 30- $\mu\text{m}$ -thick ribbons of both alloys have been used as both are completely amorphous in the as-spun condition. Figure 2 shows DSC thermograms of the

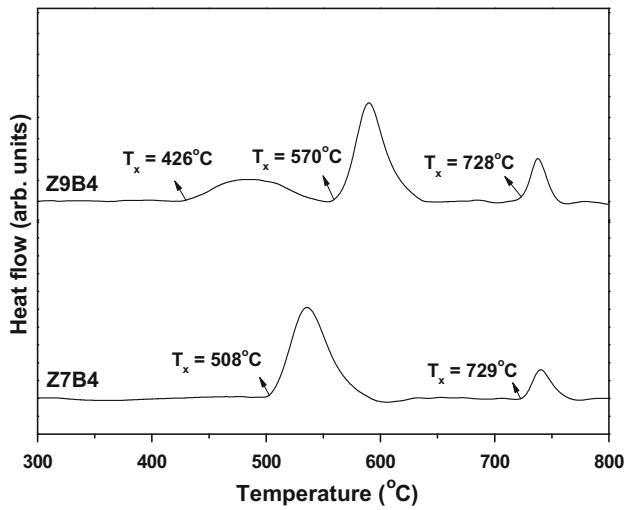


Fig. 2—DSC thermograms of Z7B4 and Z9B4 as-spun ribbons obtained at the heating rate of 20 K/min (20 °C/min).

as-spun ribbons of Z7B4 and Z9B4 ribbons obtained at a heating rate of 20 K/min (20 °C/min). The Z7B4 as-spun ribbon exhibits two exothermic peaks with onset temperatures of 781 K and 1002 K (508 °C and 729 °C), whereas the Z9B4 ribbon has three exothermic peaks with onset temperatures, namely 699 K, 843 K, and 1001 K (426 °C, 570 °C, and 728 °C), indicating a three-stage crystallization process. Figure 3(a) shows the XRD pattern of Z7B4 ribbon annealed at 813 K (540 °C) for 1 hour. The XRD pattern can be indexed with bcc  $\alpha$ -Fe phase. This indicates that the DSC peak for Z7B4 ribbon with onset at 781 K (508 °C) corresponds to the crystallization of  $\alpha$ -Fe phase. Figure 3(b) shows the XRD patterns of Z9B4 ribbon, annealed at different temperatures [773 K to 858 K (500 °C to 585 °C)]. The indexing of the ribbon annealed at 773 K (500 °C) (which is between 1st and 2nd exothermic peaks in DSC thermogram) revealed the precipitation of bcc from amorphous phase. This implies that the 1st broad DSC peak of Z9B4 ribbon with onset at 699 K (426 °C) corresponds to the crystallization of bcc  $\alpha$ -Fe phase. Comparing the result with Z7B4, it can be observed that the onset temperature of bcc phase decreases with Zr content. It is interesting to note that, although the GFA of Z9B4 is higher than that of Z7B4, the former crystallizes earlier. Indexing the XRD pattern of Z9B4 ribbon annealed at 813 K (540 °C) revealed the existence of  $\text{Fe}_2\text{Zr}$  phase (C15 Laves phase with fcc structure) along with strong peak of bcc  $\alpha$ -Fe phase. Further heat treating the ribbon at 858 K (585 °C), the XRD peak intensity of  $\text{Fe}_2\text{Zr}$  phase is found to be high as compared to that of bcc phase. Since no other phase was found by indexing the XRD pattern of ribbon annealed at 858 K (585 °C), the 2nd DSC peak of Z9B4 ribbon with onset at 843 K (570 °C) can be assigned to be the crystallization of  $\text{Fe}_2\text{Zr}$  phase. Detailed structural evolution of these two ribbons at different conditions and their crystallization temperatures are shown in Table I. Further, it can be observed that onset temperature of 2nd exothermic peak of Z7B4

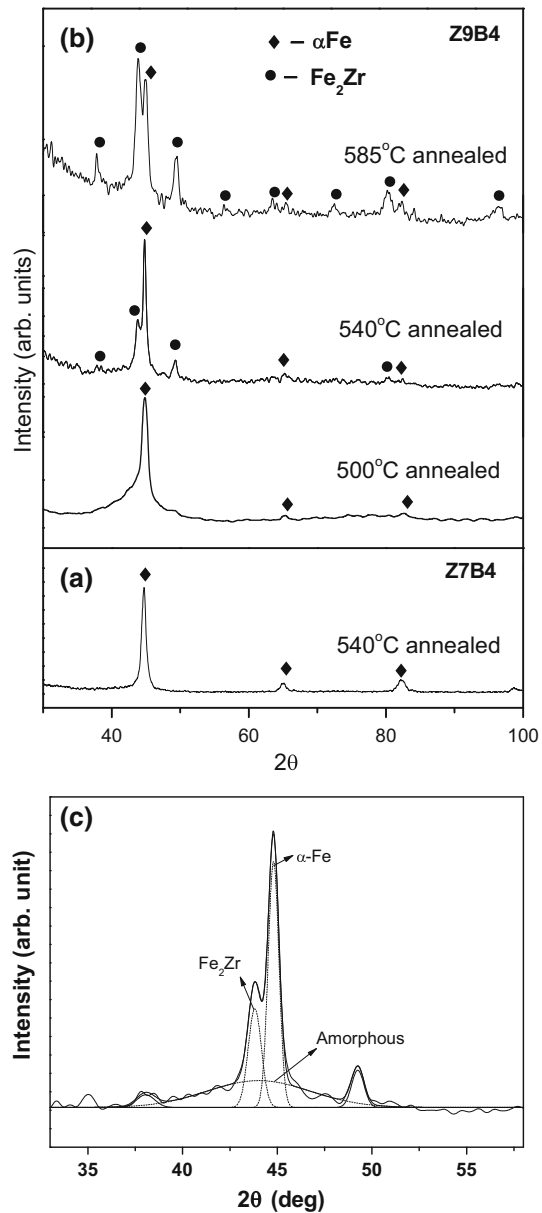


Fig. 3—XRD patterns of annealed ribbons of (a) Z7B4 and (b) Z9B4 alloys and (c) deconvolution of intense XRD peak of 813 K (540 °C) temperature-annealed Z9B4 ribbon.

ribbon [1002 K (729 °C)] and 3rd exothermic peak of Z9B4 ribbon [1001 K (728 °C)] are almost same. Comparing our results with the reported literature, it can be concluded that this higher temperature exothermic peak for both Z7B4 and Z9B4 ribbons corresponds to the formation  $\text{Fe}_3\text{Zr}$  phase (C14 Laves phase) from the residual amorphous matrix.<sup>[12]</sup>

The precision lattice parameters ( $a_0$ ) have been determined using Nelson–Riley (N–R) extrapolation method<sup>[13]</sup> in which lattice parameter, calculated from each peak, is plotted against the N–R function  $((\cos^2\theta/\sin\theta) + (\cos^2\theta/\theta))$ . A straight line is drawn by regression analysis and extrapolated up to zero value of N–R function. The intercept value gives the measure of the precision lattice parameter. The  $a_0$  values of different

**Table I. Physical Properties of the As-Spun and Annealed Ribbons of Z7B4 and Z9B4 Alloys**

Alloy	As Spun/ Annealed	Structure	DSC Results: Crystallization Temperature ( $\pm 1$ K)					Mössbauer Results: Hyperfine Field (kOe) Peak					Thermomagnetic Results: Curie Temperature ( $\pm 1$ K)	
			$T_{x1}$	$T_{x2}$	$T_{x3}$	1st Amor	2nd Fe <sub>2</sub> Zr	3rd Fe <sub>2</sub> Zr	4th Interface	5th bcc	$T_{c1}$ (°C) Amor	$T_{c2}$ (°C) Fe <sub>2</sub> Zr		
Z7B4	as spun	amor	781 K (508 °C)	—	1002 K (729 °C)	90	—	—	—	—	—	329 K (56 °C)	—	
	813 K (540 °C)	amor + $\alpha$ -Fe	—	—	—	130 $\pm$ 0.61	—	266 $\pm$ 1.04	324 $\pm$ 0.10	—	—	—	—	
Z9B4	as spun	amor	699 K (426 °C)	843 K (570 °C)	1001 K (728 °C)	88.0	—	—	—	—	—	346 K (73 °C)	—	
	773 K (500 °C)	amor + bcc	—	—	—	86.0 $\pm$ 1.39	—	249 $\pm$ 0.19	286 $\pm$ 0.16	—	—	—	—	
	813 K (540 °C)	amor + bcc + Fe <sub>2</sub> Zr	—	—	—	91.0 $\pm$ 0.78	177 $\pm$ 0.97	216 $\pm$ 0.85	neg	324 $\pm$ 0.21	374 K (101 °C)	449 K (176 °C)	—	
	(858 K) 585 °C	amor + $\alpha$ -Fe + Fe <sub>2</sub> Zr	—	—	—	91.5 $\pm$ 0.081	174 $\pm$ 0.62	212 $\pm$ 0.73	neg	324 $\pm$ 0.16	393 K (120 °C)	475 K (202 °C)	—	

specimens are given in Table II. The  $a_0$  value of bcc phase of Z7B4 ribbon, annealed at 813 K (540 °C), is 2.8586 Å which is close to the  $a_0$  of pure Fe (2.86 Å). In case of Z9B4 ribbon, the  $a_0$  value of specimen annealed at 773 K (500 °C) is 2.8710 Å, whereas it becomes 2.8569 and 2.8587 Å for the specimens annealed at 813 K and 858 K (540 °C and 585 °C), respectively.

The activation energy of crystallization ( $E$ ) was calculated from DSC thermograms obtained at different heating rates using Kissinger method.<sup>[14]</sup> The slope of plot of  $\ln(\beta/T_p^2)$  vs  $1/T_p$ , for different  $\beta$  (heating rate) values, multiplied by universal gas constant yields the activation energy, where  $T_p$  is peak temperature of the transformation. The activation energy of all phases is also shown in Table II. The activation energy of phase transformation corresponding to bcc phase for Z7B4 and Z9B4 is 299 and 64 kJ/mol, respectively, whereas the activation energy of phase transformation corresponding to Fe<sub>2</sub>Zr phase in Z9B4 alloy is 351 kJ/mol.

The enthalpy of crystallization per mol ( $\Delta H$ ) for all phases has been evaluated from the area under the crystallization peak of DSC thermogram divided by the molecular weight of the particular phase. Again the weight fraction of individual phase was calculated from the volume fraction multiplied by the density of the respective phase. The volume fractions of  $\alpha$ -Fe ((110) peak), Fe<sub>2</sub>Zr ((440) peak), and residual amorphous phase have been obtained from the area fraction of different phases which had been evaluated by deconvoluting the intense overlapping peak in the XRD patterns of annealed Z7B4 and Z9B4 ribbons. Figure 3(c) shows a typical deconvolution of intense XRD peak of Z9B4 ribbon annealed at 813 K (540 °C). The densities of  $\alpha$ -Fe and Fe<sub>2</sub>Zr, obtained from the literature, are 7.87<sup>[15]</sup> and 7.82 g/cc, respectively.<sup>[16]</sup> Table II gives the calculated volume fraction of  $\alpha$ -Fe, and residual amorphous phases for Z7B4 ribbon annealed at 813 K (540 °C) and  $\alpha$ -Fe, Fe<sub>2</sub>Zr and residual amorphous phases for Z9B4 ribbon annealed at 858 K (585 °C). The  $\Delta H$  per mol calculated for bcc  $\alpha$ -Fe and Fe<sub>2</sub>Zr phases of Z9B4 ribbon are also shown in Table I. It can be observed that the enthalpy of bcc  $\alpha$ -Fe phase reduces drastically with Zr content.

### B. Transmission Electron Microscopy

Figures 4(a) and (b) show TEM bright field (BF) micrographs of the as-spun and 813 K (540 °C) annealed ribbons of Z7B4 alloy, respectively. The insets in both the figures show the selected area diffraction (SAD) pattern of the respective regions. The featureless contrast in Figure 4(a) and corresponding halo ring in SAD pattern indicate that the as-spun ribbon is fully amorphous. The BF image of Z7B4 ribbon annealed at 813 K (540 °C) shows the nanocrystalline precipitates in a featureless matrix (Figure 4(b)). The indexing of the corresponding ring pattern in SAD has revealed the formation of bcc  $\alpha$ -Fe phase from the amorphous matrix. The size of these grains was measured within a BF image area of 500 nm  $\times$  600 nm for about 100 to 200 grains, and the histogram of grain size distribution has been plotted and is shown in Figure 4(c). The



**Table II. Calculated Volume Fraction of Phases, Activation Energy, Enthalpy, Grain Size, and Mössbauer Fitting Parameters of the As-Spun and Annealed Ribbons of Z7B4 and Z9B4 Alloys**

Alloy	As Spun/ Annealed	Thermal analysis										Histogram				Deconvolution of Hyperfine Field: Spectral Contribution (pct)				
		Precision Lattice Parameter Values of bcc $\alpha$ -Fe Phase (Å)		Deconvolution of XRD Volume Fraction (pct)		Activation Energy, $E$ (kJ/mol)		Enthalpy, $\Delta H$ (kJ/mol)		of Grain Size Distribution Obtained from TEM (nm)		FWHM		Amor		Fe <sub>2</sub> Zr		Inter Face		
		Amor	bcc	Fe <sub>2</sub> Zr	bcc	Fe <sub>2</sub> Zr	bcc	Fe <sub>2</sub> Zr	bcc	Fe <sub>2</sub> Zr	FW	HM	FW	HM	FW	HM	Fe <sub>2</sub> Zr	Fe <sub>2</sub> Zr	Inter Face	bcc
Z7B4	as spun	—	—	—	—	—	—	—	—	—	—	—	—	—	—	—	—	—	—	—
	813 K (540 °C)	2.8586	66	—	—	—	—	—	—	—	—	—	—	—	—	—	—	—	8	63.8
Z9B4	as spun	—	—	—	—	—	—	—	—	—	—	—	—	—	—	—	—	—	—	—
	773 K (500 °C)	2.8710	31.6	—	—	—	—	—	—	—	—	—	—	—	—	—	—	—	—	—
	813 K (540 °C)	2.8569	38.2	20.3	—	—	—	—	—	—	—	—	—	—	—	—	—	—	—	—
	858 K (585 °C)	2.8587	34	42.6	—	—	—	—	—	—	—	—	—	—	—	—	—	—	—	—

histogram was fitted with Lorentzian distribution curve and the fitted parameters are given in Table II. The average grain size ( $d_{av}$ ) obtained from the histogram is found to be 7.8 nm with a scatter in the grain size (FWHM) of 3 nm.

Figure 5(a) shows the BF image of Z9B4 as-spun ribbon and the inset is the corresponding SAD pattern. In this case also, the featureless contrast in BF image and corresponding halo ring in the SAD pattern reveal the presence of fully amorphous phase. Figure 5(b) shows the BF image of Z9B4 ribbon annealed at 773 K (500 °C) with the corresponding SAD pattern as inset. One can observe the formation of uniformly distributed nanocrystalline grains which have been indexed as bcc  $\alpha$ -phase in the remaining amorphous matrix. Figure 5(c) shows the histogram of grain size distribution for Z9B4 ribbon annealed at 773 K (500 °C) which has been evaluated in the similar way to that for annealed Z7B4 ribbon. The parameters using Lorentzian fitting are given in Table II. The average grain size is 9.1 nm with the scatter in the grain size of 3.2. One can observe that the average grain size of bcc  $\alpha$ -Fe phase in Z9B4 ribbon annealed at 773 K (500 °C) is larger than that the one obtained in Z7B4 ribbon annealed at 813 K (540 °C).

Figure 5(d) shows the BF image and corresponding SAD pattern (inset) of Z9B4 ribbon annealed at 813 K (540 °C) revealing that the number density and size of nanocrystalline grains have increased considerably as compared to that of ribbon annealed at 773 K (500 °C). The indexing of SAD pattern has revealed the existence of Fe<sub>2</sub>Zr phase along with bcc  $\alpha$ -phase. The fitted histogram of grain size (Figure 5(e)) shows a bimodal distribution with smaller grains having the average grain size of 5.3 nm and bigger grains having the average grain size of 14 nm (Table II). Figures 5(f) and (g) show BF image of ribbon annealed at 858 K (585 °C) with SAD pattern as inset and corresponding histogram of grain size respectively. Figure 5(g) also shows bimodal distribution of grain size with smaller grains having the average grain size of 11.6 nm and the bigger ones having the average grain size of 33 nm. The electron dispersive X-ray analysis (EDAX) results obtained from the bigger grain (33 nm) revealed the composition to be, Fe: 99.06, Zr: 0.66 and Cu: 0.28 at. pct. The composition of smaller grains could not be measured accurately because of the interference from the contribution of surrounding amorphous phase.

### C. Magnetic Properties

Figures 6(a) and (b) show the Mössbauer spectra of the as-spun and 813 K (540 °C) annealed Z7B4 ribbons, respectively. All recorded spectra were analyzed using Leacser program to get probability distribution of magnetic hyperfine fields  $P(H)$ . Figures 6(c) and (d) show the probability distribution of hyperfine field of the as-spun and annealed Z7B4 ribbons corresponding to Figures 6(a) and (b), respectively. The as-spun Z7B4 ribbon shows a broad peak in hyperfine field distribution at 90 kOe which is the characteristic of amorphous phase and similar to the results published elsewhere.<sup>[17,18]</sup> The probability distribution of hyperfine

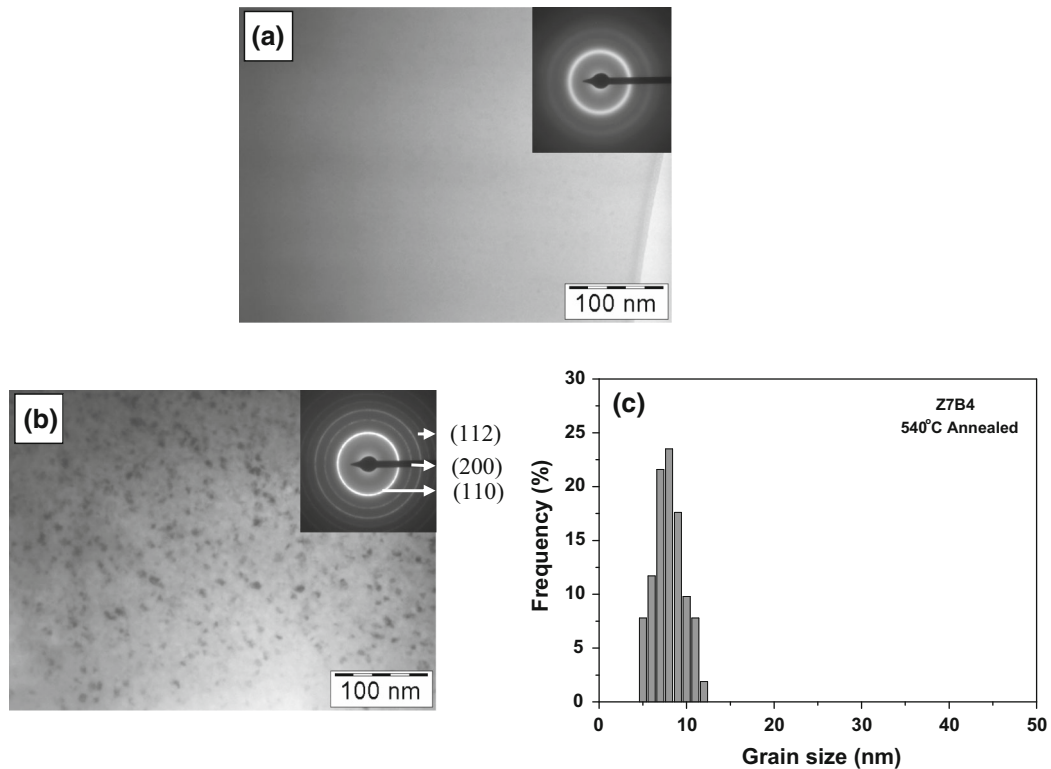


Fig. 4—TEM bright field image of Z7B4 ribbons; (a) as-spun condition, (b) 813 K (540 °C) annealed condition (insets show corresponding SAD patterns), and (c) histogram of grain size distribution of 813 K (540 °C) annealed sample.

field of ribbon annealed at 813 K (540 °C) exhibits three peaks, namely a sharp and intense peak at 325 kOe and broad and low intensity peaks at 266 and 131 kOe, respectively. The peak at 325 kOe is due to the presence of  $\alpha$ -Fe phase, whereas the peak at 266 kOe can be attributed to contribution from the interface of bcc  $\alpha$ -Fe and amorphous phase and the peak at 131 kOe can be assigned to the contribution from residual amorphous phase.

Figures 7(a) through (d) show the Mössbauer spectra of the as-spun, 773 K, 813 K, and 858 K (500 °C, 540 °C, and 585 °C), annealed ribbons of Z9B4 alloy, respectively. The corresponding probability distributions of hyperfine field are shown in Figures 7(e) through (h), respectively. Similar to Z7B4 ribbon, the hyperfine field distribution (Figure 7(e)) of the as-spun Z9B4 ribbon exhibits a broad peak at 88 kOe, which is the typical characteristics of amorphous phase. In case of hyperfine field distribution of Z9B4 ribbon annealed at 773 K (500 °C) (Figure 7(f)), two small peaks can be observed at 287 and 249 kOe, in addition to the amorphous peak at 86 kOe. These small peaks at 287 and 249 kOe may be attributed to the contribution from the Fe-based bcc solid solution and interface between the amorphous and bcc phase, respectively. Due to the presence of alloying elements such as Zr, B, and Cu, inside the bcc  $\alpha$ -Fe lattice, the hyperfine field value of Fe-based bcc solid solution (287 kOe) is far less than that of pure Fe (330 kOe). The hyperfine field distribution of Z9B4 ribbon annealed at 813 K (540 °C) is

shown in Figure 7(g). In addition to the amorphous peak at 91 kOe and almost pure Fe phase peak at 324 kOe, two kinks at 184 and 221 kOe can be observed. These are attributed to two distinguishable iron sites in  $\text{Fe}_2\text{Zr}$  phase.<sup>[19]</sup> It can be pointed out that the contribution from interface could not be deconvoluted. Figure 7(h) shows the hyperfine field distribution of ribbon annealed at 858 K (585 °C) which is almost similar to that of ribbon annealed at 813 K (540 °C) except for the fact that the intensities of hyperfine field correspond to  $\text{Fe}_2\text{Zr}$  phase have increased.

Figure 8(a) shows the thermomagnetic curves (obtained at 500 Oe applied field) of the as-spun and 813 K (540 °C) annealed ribbon of Z7B4 alloy up to 823 K (550 °C). In case of the as-spun ribbon, one can observe that the thermomagnetic curve suddenly drops down at 329 K (56 °C), remains constant at near zero value up to around 773 K (500 °C), and then increases sharply. The initial decrease of thermomagnetic curve is associated with the ferro to paramagnetic transition ( $T_c$ ) of amorphous phase, whereas the sharp increase in magnetization at high temperature is associated with the crystallization of  $\alpha$ -Fe phase whose Curie temperature ( $T_c$ ) is higher than 823 K (550 °C). The magnetization of annealed ribbon shows a monotonous decrease till 823 K (550 °C).

Figure 8(b) shows the thermomagnetic curves of the as-spun and different temperature-annealed Z9B4 ribbons. The magnetization behavior of the as-spun Z9B4 ribbon is similar to that of the as-spun Z7B4 ribbon. The Curie temperature of amorphous phase is 346 K

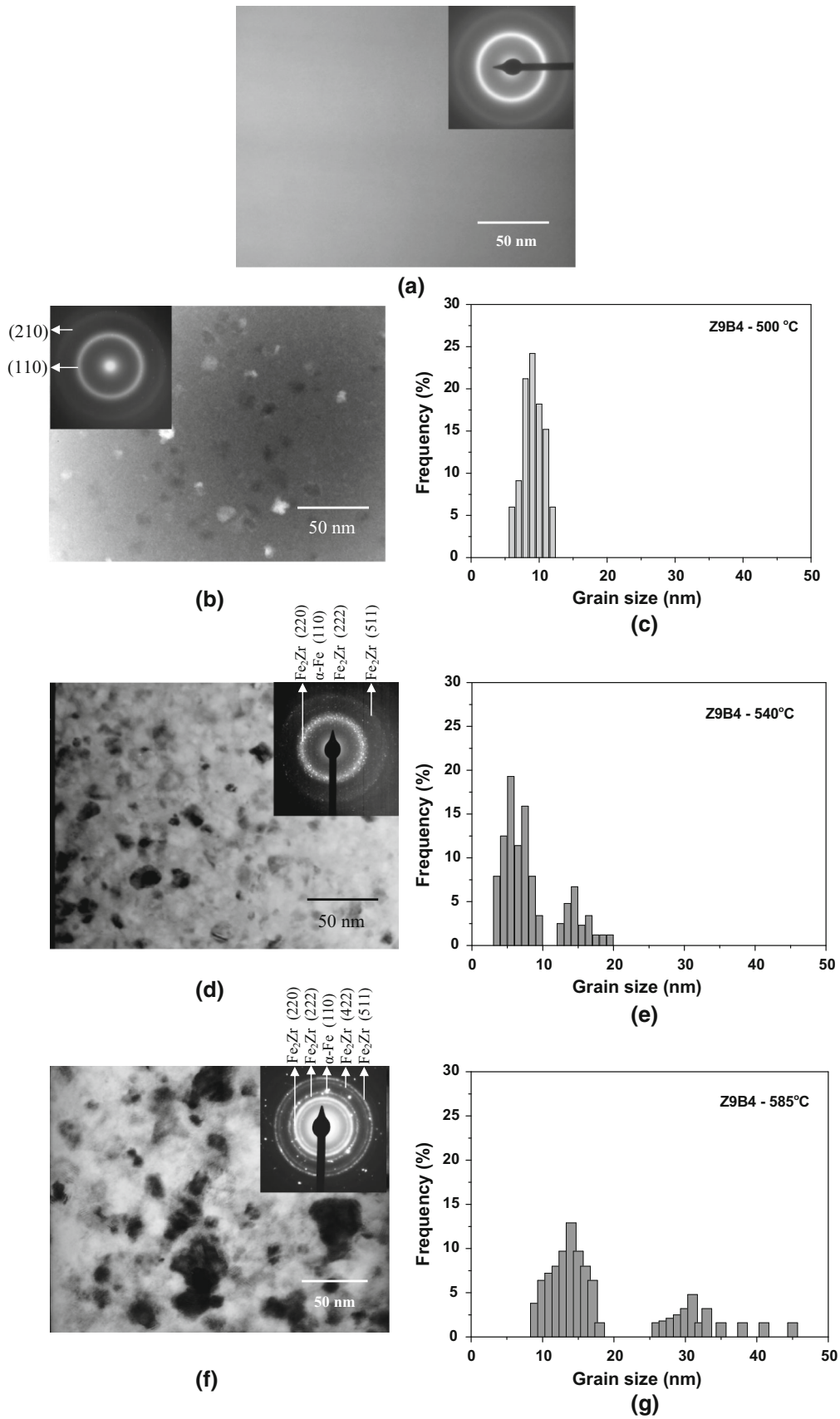


Fig. 5—TEM bright field images of the as-spun ribbon (a) and ribbons annealed at 773 K (500 °C) (b), 813 K (540 °C) (d), and 858 K (585 °C) (f) of Z9B4 alloy. The corresponding histograms of grain size distribution of ribbons annealed at 773 K (500 °C) (c), 813 K (540 °C) (e) and 858 K (585 °C) (g). The insets show corresponding SAD patterns.

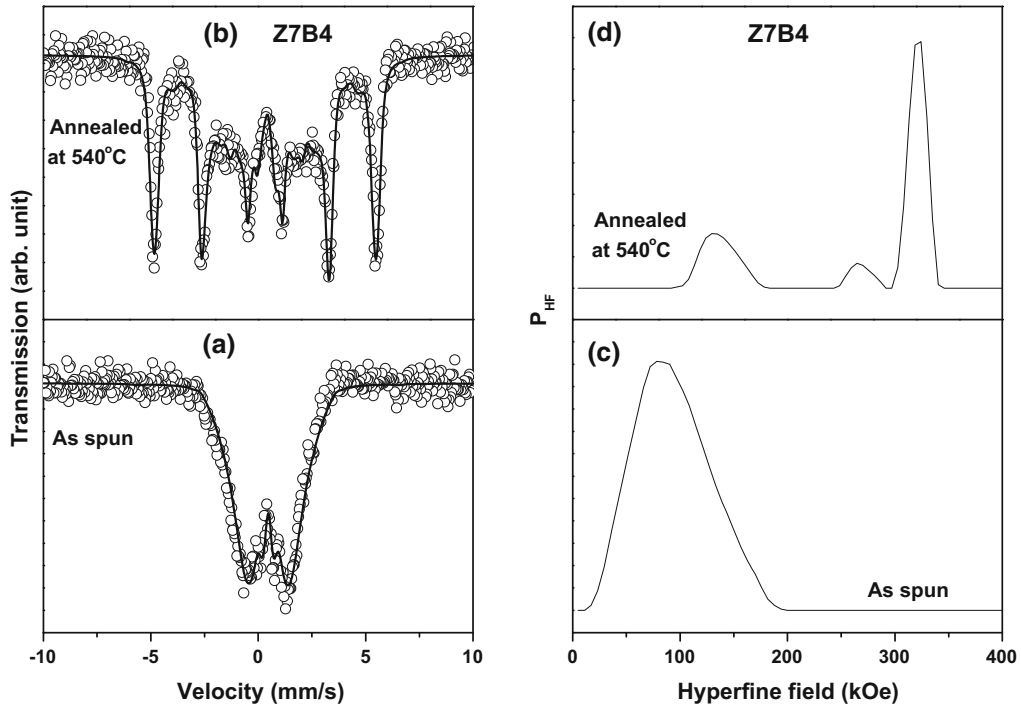


Fig. 6—Mössbauer spectra of Z7B4 ribbons: (a) as-spun and (b) 813 K (540 °C) annealed conditions. The corresponding probable distribution of hyperfine field for the (c) as-spun and (d) 813 K (540 °C) annealed ribbons.

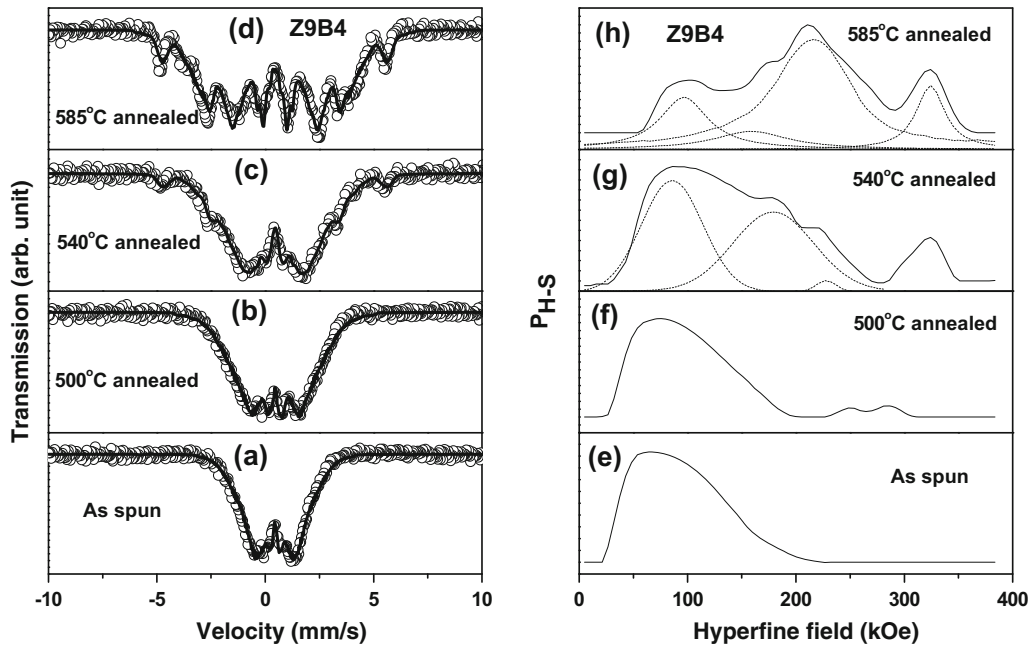


Fig. 7—Mössbauer spectra of Z9B4 ribbons: (a) as-spun ribbon and ribbons annealed at (b) 773 K (500 °C), (c) 813 K (540 °C), and (d) 858 K (585 °C). The corresponding probable distribution of hyperfine field for (e) as-spun ribbon and ribbons annealed at (f) 773 K (500 °C), (g) 813 K (540 °C) and (h) 858 K (585 °C).

(73 °C), whereas the crystallization of  $\alpha$ -Fe phase from amorphous matrix is 808 K (535 °C). The thermomagnetic curve of ribbon annealed at 813 K (540 °C) shows a 1st Curie temperature around 374 K (101 °C),

subsequently forms a step followed by dropping down the magnetization value up to 0.1 T around 349 K (176 °C) (second  $T_c$ ), and then remains almost the same up to 823 K (550 °C). The thermomagnetic curve of



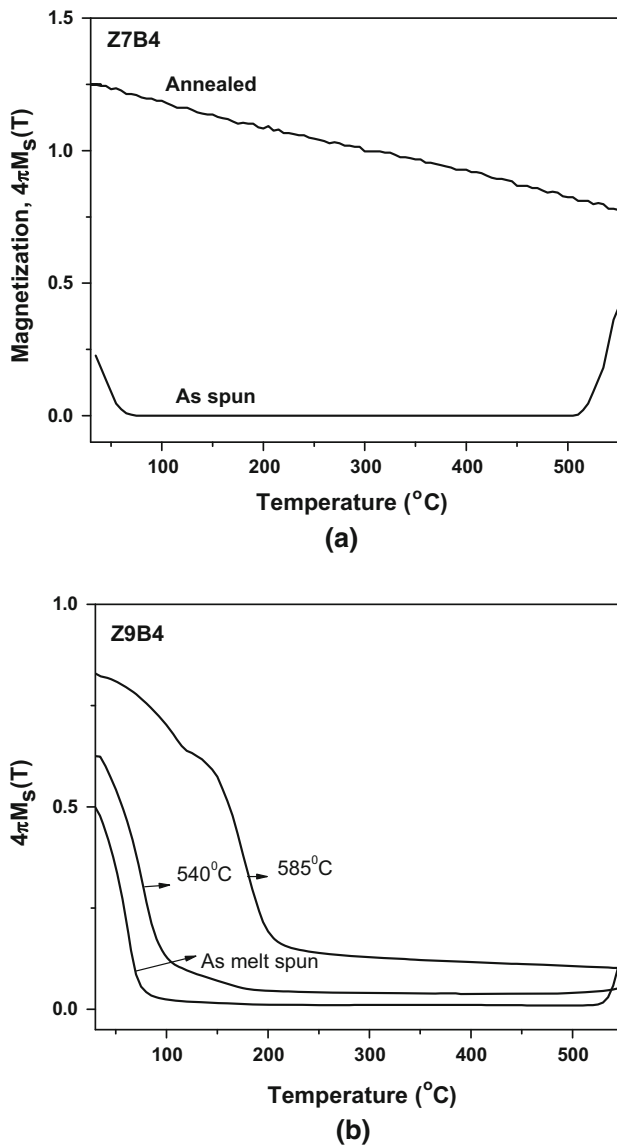


Fig. 8—Thermomagnetic curves (500 Oe field) of the as-spun ribbon and annealed ribbons of (a) Z7B4 and (b) Z9B4 ribbons.

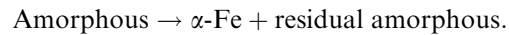
ribbon annealed at 858 K (585 °C) also shows two  $T_c$ : the first kink around 393 K (120 °C) and other around 475 K (202 °C). The magnetization curve then reaches at 0.2 T and remains almost the same up to 823 K (550 °C).

#### IV. DISCUSSION

##### A. Phase Transformation

Our results indicate that upon heating, the amorphous phase in both Z7B4 and Z9Z4 has partially been transformed into bcc phase. In case of Z7B4 ribbon, the detailed Mössbauer analysis has revealed the hyperfine field of bcc phase in ribbon annealed at 813 K (540 °C) is as high as 325 kOe. Comparing the hyperfine field value of pure  $\alpha$ -Fe to be 330 kOe, it can be inferred that the composition of bcc phase is close to pure Fe which

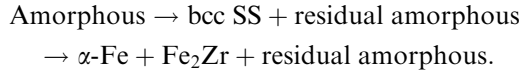
has less amount of other alloying elements such as Zr, B, and Cu. Therefore, it can be concluded that the crystallization of amorphous Z7B4 ribbon occurred through the following sequence:



The crystallization behavior of Z9B4 ribbon is different from that of Z7B4 ribbon. In this case, annealing at 773 K (500 °C) which is above the 1st crystallization peak obtained from DSC thermogram resulted in forming bcc phase. Large differences in crystallization temperatures and the enthalpies of crystallization between bcc phases obtained in both annealed Z7B4 and Z9B4 ribbons reveal that the compositions are different. This observation is complemented with the Mössbauer spectroscopy result where the hyperfine field of bcc phase in Z9B7 ribbon annealed at 773 K (500 °C) is found to be less (287 kOe) than that for annealed Z7B4 ribbon. From this result, it can be inferred that the bcc phase in Z9B4 ribbon annealed at 813 K (540 °C) is Fe-based solid solution (SS) which contains alloying elements such as Zr, B, and Cu. This is also supported by the low value of activation energy (64 kJ/mol) of bcc SS revealing the ease of crystallization. Since the kinetics of crystallization process for bcc phases in both ribbons is different, the average grain size of bcc SS obtained in Z9B4 ribbon annealed at 773 K (500 °C) (9.1 nm) is found to be larger than that of bcc phase of Z7B4 ribbon annealed at 813 K (540 °C) (7.8 nm).

Although the second crystallization temperature of Z9B4 ribbons obtained from DSC measurements at a heating rate of 20 °C/min is ~843 K (570 °C), the thermomagnetic measurements revealed that the magnetization increases sharply at 808 K (535 °C) due to the crystallization of  $\alpha$ -Fe phase. Both XRD and TEM studies indicate that increasing the annealing temperature to 813 K (540 °C) and then to 858 K (585 °C) resulted in the precipitation of both  $\alpha$ -Fe and  $\text{Fe}_2\text{Zr}$  phases. The value of activation energy, as high as 351 kJ/mol, reveals the higher stability of the phases. The hyperfine field peak around 287 kOe that could be observed due to the formation of iron solid solution during decomposition of amorphous phase when Z9B4 ribbon is annealed at 773 K (500 °C) could not be observed when annealed at these higher temperatures. Instead a new peak around 324 kOe appears. This corresponds to hyperfine field of pure Fe. This suggests that with the increase in annealing temperature, alloying elements such as Zr, B, and Cu get partitioned from the bcc Fe phase. The results also corroborate with the precision lattice parameter ( $a_0$ ) calculations. The  $a_0$  value for Z9B4 ribbon annealed at 773 K (500 °C) is higher (2.8710 Å) than that of ribbons annealed at high temperatures (2.8569 to 2.8587 Å) and Z7B4 ribbon annealed at 813 K (540 °C) (2.8586 Å). This implies the presence of other alloying elements in bcc phase of Z9B4 ribbon annealed at 773 K (500 °C) which get partitioned at higher annealing temperatures. The bimodal distribution of grain size observed in bright field TEM micrographs was further explored. The detailed EDAX analysis reveals that the bigger grains are almost

pure Fe. The value of enthalpy estimated from the second exothermic peak is 28.8 kJ/mol. Therefore, a suggested pathway for the three-stage phase transformation process is as follows:



## B. Phase Stability

The results presented show significant difference in the decomposition behavior of amorphous phase in the two ribbons where the chemical composition differs by 2 at. pct Zr. To understand the phase stability in Z7B4 and Z9B4 alloys, the molar Gibbs free energies of amorphous ( $G_m^{\text{amor}}$ ), bcc ( $G_m^{\text{bcc}}$ ), and  $\text{Fe}_2\text{Zr}$  ( $G_m^{\text{Fe}_2\text{Zr}}$ ) phases have been calculated based on regular solution model. Since only 1 at. pct Cu has been added in both alloys, the calculation of molar free energy of all phases has been simplified by omitting Cu in the solution. Therefore, in the present study, only Fe-Zr-B ternary alloy system has been considered. Accordingly,  $G$  of any phase ( $\phi$ ) can be defined as<sup>[20]</sup>

$$\begin{aligned} G_m^\phi &= x_B G_B^\phi + x_{\text{Fe}} G_{\text{Fe}}^\phi + x_{\text{Zr}} G_{\text{Zr}}^\phi \\ &+ RT(x_B \ln x_B + x_{\text{Fe}} \ln x_{\text{Fe}} + x_{\text{Zr}} \ln x_{\text{Zr}}) \\ &+ x_B x_{\text{Fe}} L_{\text{B,Fe}}^\phi + x_B x_{\text{Zr}} L_{\text{B,Zr}}^\phi + x_{\text{Fe}} x_{\text{Zr}} L_{\text{Fe,Zr}}^\phi \\ &+ x_B x_{\text{Fe}} x_{\text{Zr}} L_{\text{B,Fe,Zr}}^\phi, \end{aligned} \quad [2]$$

where  $x_i$  (where  $i = \text{Fe/Zr/B}$ ) is the mole fraction of the  $i$ th element,  $G_i^\phi$  is the Gibbs free energy of the  $i$ th element in  $\phi$  phase,  $R$  is the gas constant,  $T$  is the temperature,  $L_{ij}^\phi$  is interaction energy between  $i$  and  $j$  elements in  $\phi$  phase, and  $L_{\text{B,Fe,Zr}}^\phi$  is the interaction energy between B, Fe, and Zr elements. It is to be noted that the ternary interaction between B, Fe, and Zr is not considered in this study. The Gibbs free energy values ( $G_i^\phi$ ) of B, Zr, and Fe were taken from thermodynamical data of various elements compiled by Hultgreen *et al.*<sup>[21]</sup> The interaction energy between  $i$  and  $j$  elements in the  $\phi$  phase was calculated using Redlich–Kister polynomial of  $n$ th degree using the formula as<sup>[22]</sup>

$$\begin{aligned} L_{ij}^\phi &= L_{ij}^\phi(0) + L_{ij}^\phi(1)(x_i - x_j)^2 + L_{ij}^\phi(2)(x_i - x_j)^2 + \dots \\ &+ L_{ij}^\phi(n)(x_i - x_j)^n, \end{aligned} \quad [3]$$

where

$$L_{ij}^\phi = a_n + b_n T. \quad [4]$$

Since amorphous phase is considered to be as a supercooled liquid whose structure is similar to that of liquid, the  $G_m^{\text{amor}}$  has been calculated from the liquid free energy data of Fe, Zr, and B and extrapolated to the supercooled region even up to room temperature.

For calculating the  $G_m^{\text{Fe}_2\text{Zr}}$ , a sublattice model has been used. Since the  $\text{Fe}_2\text{Zr}$  is a Laves phase consisting of C15 structure with varying composition, sublattice with the formula of  $(\text{Fe,Zr})_2(\text{Fe,Zr})_1$  has been considered for the calculation. Therefore, the molar Gibbs free energy of  $\text{Fe}_2\text{Zr}$  ( $G_m^{\text{Fe}_2\text{Zr}}$ ) can be obtained using the following formula<sup>[20]</sup> as

$$\begin{aligned} G_m^{\text{Fe}_2\text{Zr}} &= y_{\text{Fe}}^{(1)} \left( y_{\text{Fe}}^{(2)} G_{\text{Fe:Fe}}^{\text{Fe}_2\text{Zr}} + y_{\text{Zr}}^{(2)} G_{\text{Fe:Zr}}^{\text{Fe}_2\text{Zr}} \right) \\ &+ y_{\text{Zr}}^{(1)} \left( y_{\text{Fe}}^{(2)} G_{\text{Zr:Fe}}^{\text{Fe}_2\text{Zr}} + y_{\text{Zr}}^{(2)} G_{\text{Zr:Zr}}^{\text{Fe}_2\text{Zr}} \right) \\ &+ mRT \left( y_{\text{Fe}}^{(1)} \ln y_{\text{Fe}}^{(1)} + y_{\text{Zr}}^{(1)} \ln y_{\text{Zr}}^{(1)} \right) \\ &+ nRT \left( y_{\text{Fe}}^{(2)} \ln y_{\text{Fe}}^{(2)} + y_{\text{Zr}}^{(2)} \ln y_{\text{Zr}}^{(2)} \right) + \text{ex} G^{\text{Fe}_2\text{Zr}}, \end{aligned} \quad [5]$$

where  $y_i^{(1)}$  and  $y_i^{(2)}$  are the site fractions of  $i$ th element in first  $(\text{Fe,Zr})_2$  and second  $(\text{Fe,Zr})_1$  sublattices, respectively.  $G_{ij}^{\text{Fe}_2\text{Zr}}$  is the molar Gibbs free energy of  $\text{Fe}_2\text{Zr}$  compound where sublattice 1 and 2 are occupied by  $i$  and  $j$  elements, respectively. The  $\text{ex} G^{\text{Fe}_2\text{Zr}}$  is the interaction energy between unlike atoms and is given by the following formula:

$$\begin{aligned} \text{ex} G^{\text{Fe}_2\text{Zr}} &= y_{\text{Fe}}^{(1)} y_{\text{Zr}}^{(1)} \left( y_{\text{Fe}}^{(2)} L_{\text{Fe,Zr:Fe}}^{\text{Fe}_2\text{Zr}} + y_{\text{Zr}}^{(2)} L_{\text{Fe,Zr:Zr}}^{\text{Fe}_2\text{Zr}} \right) \\ &+ y_{\text{Fe}}^{(2)} y_{\text{Zr}}^{(2)} \left( y_{\text{Fe}}^{(1)} L_{\text{Fe:Fe,Zr}}^{\text{Fe}_2\text{Zr}} + y_{\text{Zr}}^{(1)} L_{\text{Zr:Fe,Zr}}^{\text{Fe}_2\text{Zr}} \right), \end{aligned} \quad [6]$$

where  $L_{ijk}^{\text{Fe}_2\text{Zr}}$  is the interaction parameter between unlike atoms on the same sublattice and is expressed by an equation similar to Eq. [3].

Using the above equations, room temperature molar free energy ( $G$ ) for amorphous, bcc, and  $\text{Fe}_2\text{Zr}$  phases as a function of Fe content in  $(\text{Fe}_x\text{Zr}_{1-x})_{96}\text{B}_4$  alloy system has been evaluated and is shown in Figure 9. The composition of both Z7B4 and Z9B4 alloys, considered in the present investigation has also been marked in the diagram. As expected, the  $G_m^{\text{amor}}$  is always higher than that of other two phases. The  $G_m^{\text{Fe}_2\text{Zr}}$  is lower than that of bcc phase within the composition between Fe = 0.53 to 0.85 at. pct. It is interesting to note that composition of equal molar free energies of bcc and  $\text{Fe}_2\text{Zr}$  phases is 0.85 at. pct Fe which is very close to the composition of Z9B4 alloy.  $G_m^{\text{bcc}}$  phase is lower beyond this composition from which it can be concluded that the bcc phase in Z7B4 alloy is more stable whereas both bcc and  $\text{Fe}_2\text{Zr}$  can coexist in Z9B4 alloy.

The molar Gibbs free energy ( $G$ ) of amorphous, bcc, and  $\text{Fe}_2\text{Zr}$  as a function of temperature for Z7B4 and Z9B4 alloys has been evaluated and is shown in Figures 10(a) and (b), respectively. It is evident that for all phases,  $G$  decreases with temperature and  $G_m^{\text{amor}}$  for both alloys is higher than that of bcc and  $\text{Fe}_2\text{Zr}$ . Since amorphous is a non-equilibrium phase at room temperature, it will tend to transform to either bcc or  $\text{Fe}_2\text{Zr}$  phase during heating. In case of Z7B4 alloy, it can be observed from the Figure 10(a) that  $G_m^{\text{bcc}}$  is always lower than that of  $\text{Fe}_2\text{Zr}$  at all temperatures implying that the bcc phase is more stable. Therefore, one can expect the formation of only stable bcc phase during

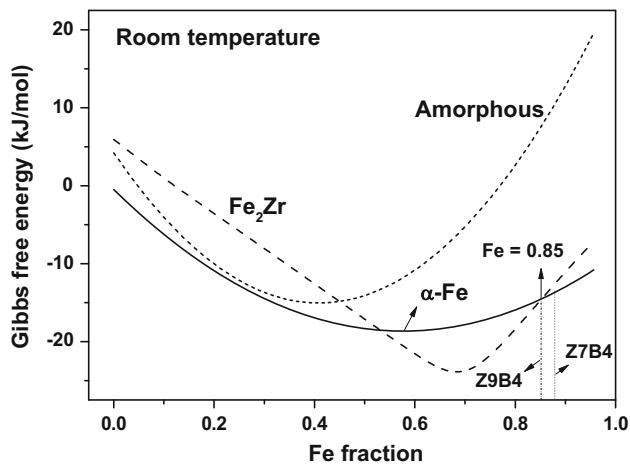


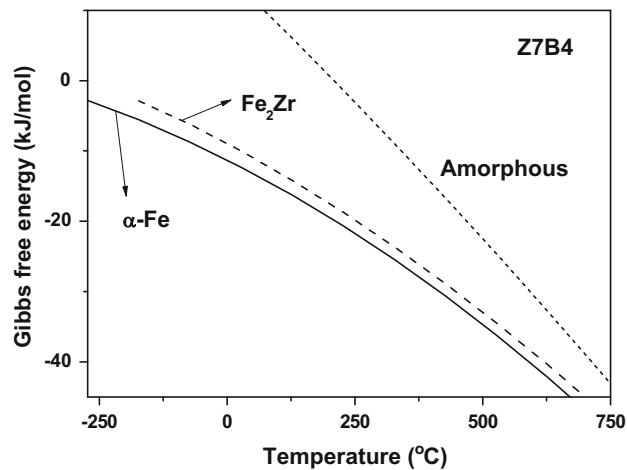
Fig. 9—Molar Gibbs free energy ( $G$ ) of amorphous,  $\alpha$ -Fe and  $\text{Fe}_2\text{Zr}$  phases as a function of Fe in  $(\text{Fe}_x\text{Zr}_{1-x})_{96}\text{B}_4$  alloy system.

annealing. In case of Z9B4 alloy (Figure 10(b)),  $G^{\text{bcc}}$  is low till 488 K (215 °C), and beyond this temperature,  $G^{\text{Fe}_2\text{Zr}}$  curve crosses over  $G^{\text{bcc}}$  and remains low throughout the higher temperature range. This implies that lower temperature favors the formation of stable bcc phase, whereas the  $\text{Fe}_2\text{Zr}$  phase is more stable at an elevated temperature. This supports our experimental observation.

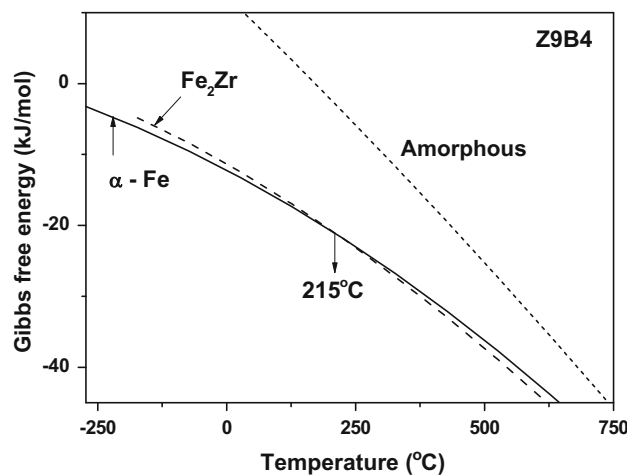
### C. Magnetic Properties

The spectral contribution of crystalline phase, amorphous phase, and  $\text{Fe}_2\text{Zr}$  phase has been calculated based on area under the curve of hyperfine field distribution peaks responsible for respective phases and is shown in Table II. Initially, the hyperfine field distribution curve is deconvoluted around each peak using Gaussian distribution curve fitting (as shown in Figures 7(g) and (h)), and the area under each peak has been calculated which gives the spectral contribution of relative Fe concentration in each phase. In case of Z7B4 ribbon annealed at 813 K (540 °C), approximately  $\frac{3}{4}$  of the total Fe atoms are contributing toward the formation of  $\alpha$ -Fe phase and the remaining  $\frac{1}{4}$  Fe atoms is retained in the amorphous phase. In case of Z9B4 ribbons, the spectral contribution of Fe atoms for bcc phase increases slowly with annealing temperature and reaches 10 pct for ribbon annealed at 858 K (585 °C). The spectral contribution of Fe atoms for  $\text{Fe}_2\text{Zr}$  phase is very high as compared to bcc  $\alpha$ -Fe phase. In amorphous phase, the spectral contribution of Fe continuously decreases at higher annealing temperature which shows that the amorphous phase is continuously getting depleted with Fe atoms. This result is well corroborated with XRD, DSC, and TEM results.

It is evident from the thermomagnetic curves of Z9B4 ribbons annealed at different temperatures that only amorphous phase  $T_c$  can be observed for the as-spun ribbon, whereas ribbons annealed at 813 K and 858 K (540 °C and 585 °C) exhibits two transition temperatures. The XRD results reveal that the phases present in



(a)



(b)

Fig. 10—Molar Gibbs free energy ( $G$ ) of amorphous,  $\alpha$ -Fe and  $\text{Fe}_2\text{Zr}$  phases as a function of temperature for (a) Z7B4 alloy and (b) Z9B4 alloy.

both the annealed samples are  $\alpha$ -Fe,  $\text{Fe}_2\text{Zr}$ , and residual amorphous phases. Since  $T_c$  of  $\alpha$ -Fe is very high [1543 K (770 °C)], the first and second transitions can be associated with the  $T_c$  of amorphous and  $\text{Fe}_2\text{Zr}$  phases, respectively. It can be observed that  $T_c$  of amorphous phase increases with annealing temperature. Although the amorphous phase is continuously depleted of Fe atoms at high annealing temperatures as shown by Mössbauer results, the exchange field penetration effect of  $\alpha$ -Fe and  $\text{Fe}_2\text{Zr}$  phase in the amorphous matrix causes an increase of amorphous phase  $T_c$ .<sup>[23,24]</sup>

The constant values of magnetization of 0.1 T in case of ribbon annealed at 813 K (540 °C) and 0.2 T in case of ribbon annealed at 858 K (585 °C) beyond the  $T_c$  of  $\text{Fe}_2\text{Zr}$  can be correlated with the existence of ferromagnetic bcc Fe phase. From the knowledge of spectral contribution, the relative Fe concentration in ribbons annealed at 813 K and 858 K (540 °C and 585 °C) are found to be 5.4 and 10 pct, respectively (Table II). Assuming that only  $\alpha$ -Fe (whose magnetization value is

2.1 T) contributes toward the magnetization at higher temperature beyond the  $T_c$  of  $\text{Fe}_2\text{Zr}$ , the magnetization values of 813 K and 858 K (540 °C and 585 °C) annealed ribbons at high temperature can be calculated to be 0.11 and 0.21 T, respectively. These are similar to the values obtained experimentally.

## V. CONCLUSIONS

The GFA (calculated using  $P_{\text{HSS}} = \Delta H^{\text{chem}}(\Delta S_{\sigma}/k_B)(\Delta S_C/R)$ ) of Z9B4 alloy is found to be higher than that of Z7B4 alloy which is validated by experimental results. On annealing, Z7B4 amorphous ribbon crystallizes to partially bcc  $\alpha$ -Fe from amorphous phase while Z9B4 amorphous ribbon crystallizes in two stages as follows: initially, partial bcc solid solution from amorphous phase followed by  $\alpha$ -Fe and  $\text{Fe}_2\text{Zr}$  phases from bcc solid solution. While annealed Z7B4 ribbon exhibits nanocrystalline bcc  $\alpha$ -Fe phase, the annealed Z9B4 ribbon exhibits the bimodal distribution of nanograins of  $\alpha$ -Fe and  $\text{Fe}_2\text{Zr}$  phases. Molar Gibbs free energy calculations using regular solution model (for amorphous and  $\alpha$ -Fe phases) and sublattice model (for  $\text{Fe}_2\text{Zr}$  intermetallic phase) reveal that the  $\alpha$ -Fe phase is a stable phase for Z7B4 alloy. In case of Z9B4 alloy, low temperature favors the formation of stable bcc phase whereas the  $\text{Fe}_2\text{Zr}$  phase is more stable at an elevated temperature.

## ACKNOWLEDGMENTS

This work was supported by Defence Research and Development Organization (DRDO), Government of India. The authors thank Dr. A. Bhattacharjee, Dr. A. K. Singh, and Dr. M. Manivel Raja of DMRL for melting alloys, XRD measurements, and Mössbauer spectroscopy, respectively. The authors gratefully acknowledge Dr. A. Gokhale, Director DMRL, and Dr. G. Malakondaiah, DS, CC (R&D) for continued support and permission to publish this work.

## REFERENCES

1. K. Suzuki, A. Makino, N. Kataoka, A. Inoue, and T. Masumoto: *Mater. Trans. JIM*, 1991, vol. 32, pp. 93–102.
2. G. Herzer: *IEEE Trans. Magn.*, 1989, vol. 25, pp. 3327–29.
3. G. Herzer and H.R. Hilzinger: *J. Mag. Mag. Mater.*, 1986, vol. 62, pp. 143–45.
4. D. Arvindha Babu, B. Majumdar, R. Sarkar, D. Akhtar, and V. Chandrasekaran: *J. Phys. D*, 2008, vol. 41, pp. 195002–195008.
5. J.C. Shih, L. Burgeos, K. Suzuki, and J.S. Garitaonanda: *J. Magn. Magn. Mater.*, 2006, vol. 304, pp. e693–96.
6. K. Hono: *Prog. Mater. Sci.*, 2002, vol. 47, pp. 621–729.
7. D. Arvindha Babu, B. Majumdar, R. Sarkar, M. Manivel Raja, and D. Akhtar: *J. Mater. Res.*, 2011, vol. 26, pp. 2065–71.
8. D. Arvindha Babu, B. Majumdar, A.P. Srivastava, B.R. Rao, D. Srivastava, B.S. Murty, and D. Akhtar: *Metal. Mater. Trans. A*, 2011, vol. 42A, pp. 508–16.
9. B.R. Rao, M. Srinivas, A.K. Shah, A.S. Gandhi, and B.S. Murty: *Intermetallics*, 2012, vol. 35, pp. 73–81.
10. B.R. Rao, A.S. Gandhi, S. Vincent, J. Bhatt, and B.S. Murty: *Trans. Ind. Inst. Metals*, 2012, vol. 65, pp. 559–63.
11. S. Vincent, B.S. Murty, and Jatin. Bhatt: *Trans. Ind. Inst. Metals*, 2012, vol. 65, pp. 827–31.
12. D.M. Zhu, K. Raviprasad, K. Suzuki, and S.P. Ringer: *J. Phys. D Appl. Phys.*, 2004, vol. 37, pp. 645–52.
13. J.B. Nelson and D.P. Riley: <http://iopscience.iop.org/0959-5309/57/3/302?fromSearchPage=true> *Proc. Phys. Soc.*, 1945, vol. 57, p. 160.
14. H.E. Kissinger: *Anal. Chem.*, 1957, vol. 29, pp. 1702–06.
15. E.A. Owen and G.I. Williams: *J. Sci. Instrum.*, 1954, vol. 31, pp. 49–54.
16. F.N. Rhines and R.W. Gould: *Adv. X-Ray Anal.*, 1962, vol. 6, pp. 62–73.
17. M. Kopcewicz, A. Grabias, and D.L. Williamson: *J. Appl. Phys.*, 1997, vol. 82, pp. 1747–58.
18. G.S. Garitaonandia, D.S. Schmoor, and J.M. Barandiran: *Phys. Rev. B*, 1998, vol. 58, pp. 12147–12158.
19. L.F. Kiss, G. Huhn, T. Kemeny, J. Balogh, and D. Kaptas: *J. Magn. Magn. Mater.*, 1996, vol. 160, pp. 229–32.
20. T. Tokunaga, K. Terashima, H. Ohtani, and M. Hasebe: *Mater. Trans.*, 2008, vol. 49, pp. 2534–40.
21. R. Hultgreen, P.D. Desai, D.T. Hawkins, M. Gleiser, K.K. Kelley, and D.D. Wagman: *Selected Value of Thermodynamic Properties of the Elements*, American Society of Metals, Materials Park, 1973, pp. 54–581.
22. O. Redlich and A.T. Kister: *Ind. Eng. Chem.*, 1948, vol. 40, pp. 345–48.
23. A. Hernando and I. Navarro: *Phys. Rev. B*, 1995, vol. 51, pp. 3281–84.
24. B. Majumdar and D. Akhtar: *Bull. Mater. Sci.*, 2005, vol. 28, pp. 395–99.